Technical Report
RAL-TR-2006-030

Knowledge Transfer of microstrip detectors; from particle to medical physics

Spyros Manolopoulos

Abstract

This project is a demonstration of Knowledge Transfer. Knowledge in the fabrication, operation and application of radiation detectors originally developed for particle physics experiments has been exploited in diverse areas of research like medical applications. Microstrip detectors, commonplace in particle physics "trackers", have been evaluated as dosimeters for radiotherapy modalities. Hospital trails conducted under the supervision of clinical scientists demonstrated the viability of these detectors as dosimeters both in the quality assurance of linear accelerators and potentially in treatment planning verification. Important quantities of interest to the clinical scientist, like depth-dose distributions, output factors, off axis ratios etc. were measured with MV X-Rays from a clinical Linac and compared with the present day standard dosimeters. All results showed the performance of our novel dosimeter to be as good as or even better than that of the hospital dosimeters. Moreover the ability of our system for dose distribution measurements in real time was proven.

1 Introduction

1.1 The microstrip detector

The microstrip is a position sensitive detector used for charged particle tracking [1]. In its generic format it comprises of a linear array of diodes, typically realised in silicon technology, where the presence of a signal in a diode well above the noise level, marks the passage of a particle, see Figure 1.

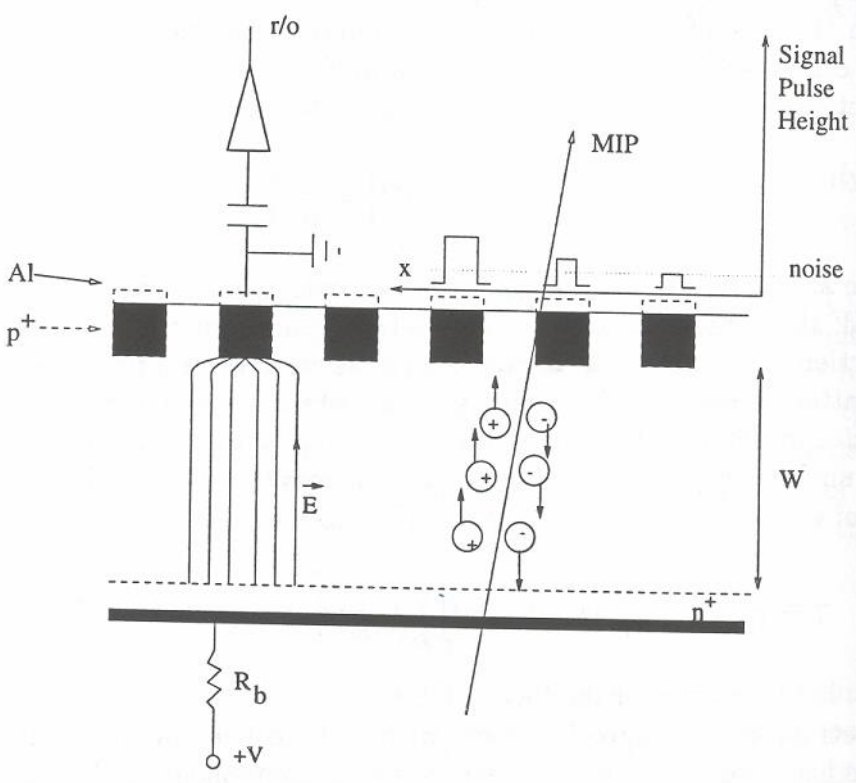

Figure 1 Schematic drawing of a microstrip detector and its principle of operation for charged particle tracking in high energy particle physics experiments [2].

The introduction of the planar process by Kemmer [3] that utilised fabrication techniques originally developed in the microelectronics industry for the manufacturing of VLSI electronics, allowed for the fabrication of reliable devices with a variety of designs (single or double sided etc.) with specialised features (e.g. integrating biasing schemes, double metal layers for one sided read-out etc.) in bulk that is with high yield and at lower cost. Since then, microstrip detectors are commonly employed in particle physics experiments for charge particle tracking with impressive performance having achieved spatial resolutions of only a few micrometers [4]. Their success has been highlighted in the forthcoming experiments at the Large Hadron Collider, where their use reached unprecedented levels. For example the CMS experiment features an all silicon tracker with approximately 10 million channels of microstrip detectors and a total active area of approximately 210 m^2 of silicon manufactured by 450 m^2 of wafer material [5].

Based on the demonstrated success of the microstrip detectors in particle physics experiments and the evident maturity of the technology could there be a merit in transferring the knowledge of their technology and capabilities to other areas of research and more importantly the health sector?

1.2 Radiotherapy

The aim of radiotherapy is the delivery of a lethal dose of radiation to a volume of diseased tissue while simultaneously sparing the surrounding healthy tissue. However, in practice there is always a trade off between the damage imparted on the diseased site versus that to the healthy tissue. In fact the basis of radiotherapy lies in the difference of the response to radiation between healthy and diseased tissue, shown in Figure 2. This illustrates the cell response, measured in terms of mortality percentage, as a function of dose for cancerous and normal cells. The position of the curve for the tumour cells, being on the left of the one for the normal cells, provides a window of opportunity for treatment since it implies that the tumour cells are killed first. Thus one has the opportunity to kill the diseased cells before radiation damage occurs to the surrounding healthy tissue. In fact, the window's "border" is defined as the dose where the damage to the healthy tissue (termed "complication" in the figure) becomes significant. This varies with radiation type and energy but also between different cells. Nonetheless, whenever a situation is encountered as the one shown in the figure, there is a possibility for cure.

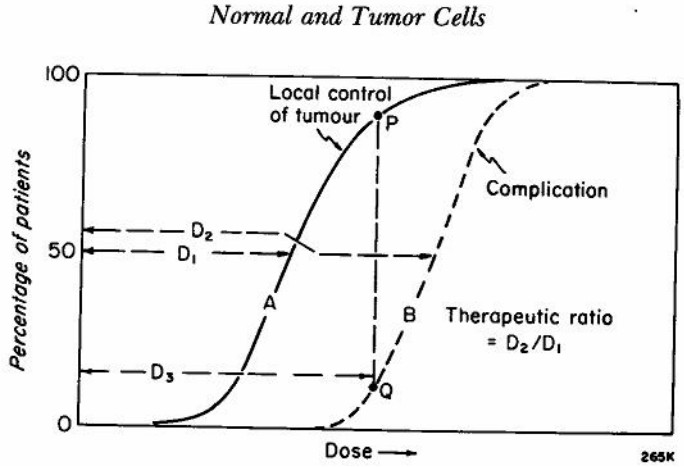

Figure 2 Illustration of the cell response for normal and tumour cells [6 Error! Reference source not found.**].**

Radiotherapy comes in two basic approaches, teletherapy (therapy from a distance) and brachytherapy (therapy in close proximity). Each encompasses a number of different modalities. In teletherapy for example one may use photons of different energies, as in MV or kV, sometimes called orthovoltage teletherapy, or even chose a different particle type, like electrons (electron MV teletherapy) or protons and ions (hadron therapy).

1.3 Stereotaxy

Stereotactic radiation therapy modalities are the radiotherapy variants of stereotactic surgery developed at UCL in 1908 by Sir Victor Horsley and Robert H. Clarke. They, like their forerunner, were developed because of the demanding requirements of (dose) localisation in the treatment of intracranial lesions [6, 7, 8]. Stereotactic radiosurgery (SRS)[1] is a single fraction treatment, whereas stereotactic radiotherapy (SRT) refers to a dose delivery in multiple fractions. Both rely on the use of a stereotactic frame, fixed on the patient's head, for the precise target localisation prior to treatment. They also utilise 3D imaging techniques, like CT or MRI, for target visualisation as well as 3D treatment planning software. The high degree of dose conformity is the trademark of both stereotactic modalities. However, due to the small target

[1] Developed by Lars Leksell in 1951.

volumes typically encountered, stringent demands are imposed on the dosimetry, which has to cope with small field sizes (less than 4 cm) and steep dose gradients at the edges of the treatment volume. The most common stereotactic techniques for dose delivery are the X-ray and gamma knife.

1.3.1 X-ray knife

This is a LINAC based technique, where multiple noncoplanar arcs of circular or dynamically shaped beams are used for the dose delivery. The beams converge on the machine's isocentre, which is stereotactically made to coincide with the centre of target. Typical energies of 6 MV are used, as more penetrating radiation is not required for head and neck treatments. The target localisation accuracy depends mainly on two factors:

- the positional accuracy of the target volume within the frame,
- the position of the frame in relation to the isocentre.

An overall accuracy of around 1mm is typically achieved between the streotactically defined target centre and the isocentre with the dominant factor being the error in the target localisation. To get an idea of the relative weight of the contributing factors, the mechanical accuracy of the isocentre is better than 0.5-0.7 mm, whereas that of the stereotactic frame centre is within 0.1 mm. The error in the target location depends on the imaging technique used during diagnosis with the best values being measured with CT, between 1.3 to 0.6 mm [6]. The picture of a typical frame for an X-ray knife is shown in the figure below. Apart form the positioning pins to the head one sees the fiducial markers, the vertical and diagonal bars on the periphery of the device that act as referencing points.

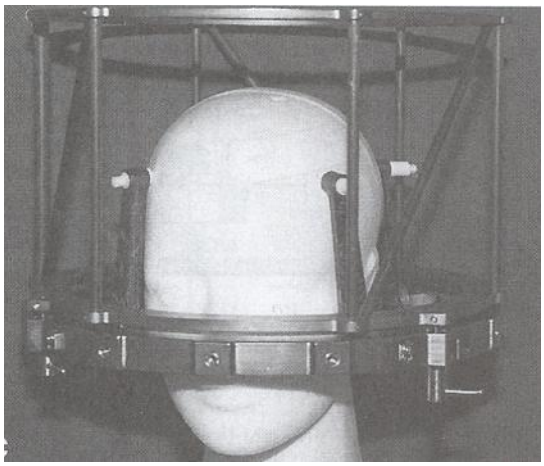

Figure 3 Basic stereotactic system, from [6].

In the next figure one sees the beam arrangement in a treatment plan for SRT with X-ray knife. In this example, five different fields are used, each in the form of an arc at different plane, representing a different gantry angle. The beams converge on the isocentre, which is made to coincide with the treatment volume's centre. Also shown are the locations of the stereotactic helmet's bars that are used for referencing and localisation purposes.

Beam collimation is achieved by the use of a tertiary collimation system, which is directly mounted below the second collimator's jaws. It features a central hole with a cone shape and a typical length of 15 cm. A number of cones with different diameters are used, ranging from 5 to 40 mm, as needed to treat the various lesions. The extension of the collimator, thus the smaller distance to the surface, results in steeper dose gradients at the edge of the field and sharper penumbras, as will be explained in the next chapter.

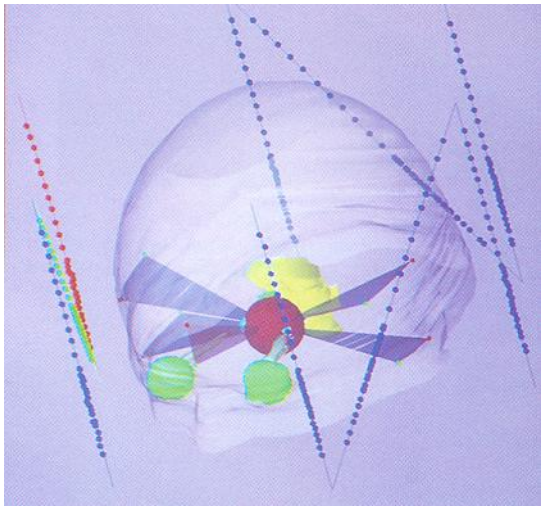

Figure 4 SRT with an X-ray knife incorporating five non-coplanar arcs. Also shown are the fiducial markers for target location through imaging (here CT), from [6].

1.3.2 Gamma knife

The gamma knife technique is used for SRS and utilises a large number of isocentric beams of gamma rays for the simultaneous irradiation of a brain lesion. This is possible by incorporating a large number (e.g. 201) of radioactive cobalrt-60 sources in a hemispherical arrangement, which are individually collimated by a specially designed helmet, as shown in the next figures.

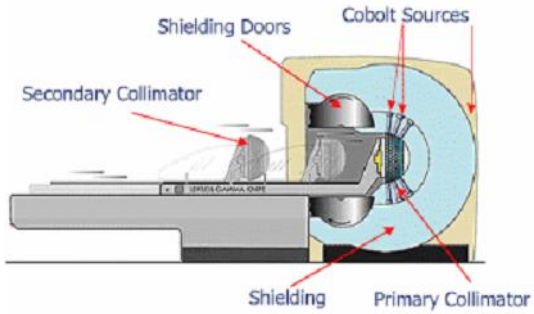

Figure 5 The gamma knife unit used at Sheffield's Weston Park hospital [12].

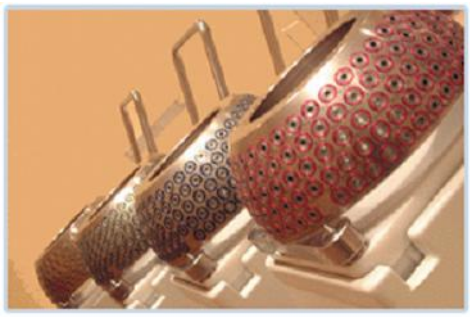

Figure 6 Detail of collimator helmets for a gamma knife system [12].

The collimator system has two parts. The primary collimator is fixed by being machined in the central body. Secondary collimation is provided by a number of interchangeable helmets with different dimensions for the channel width that produce circular fields of different size

ranging from 4 to 18 mm at the focus point ("isocentre"). The positioning accuracy of the helmets is within 0.1 mm. Selected collimator channels can be blocked to shield the eyes or optimise the dose distribution. A stereotactic helmet attached to the patient's skull is used for target localisation and positioning with respect to the isocentre.

1.3.3 Dose distributions in small fields

The dosimetric problems encountered in stereotactic techniques have brought additional demands on the dosimeter specifications due to the small size of the radiation fields and the steep penumbras, both of which are key ingredients for the success of these radiotherapy modalities. An example of typical dose distributions encountered with stereotactic beams is shown in Figure 7.

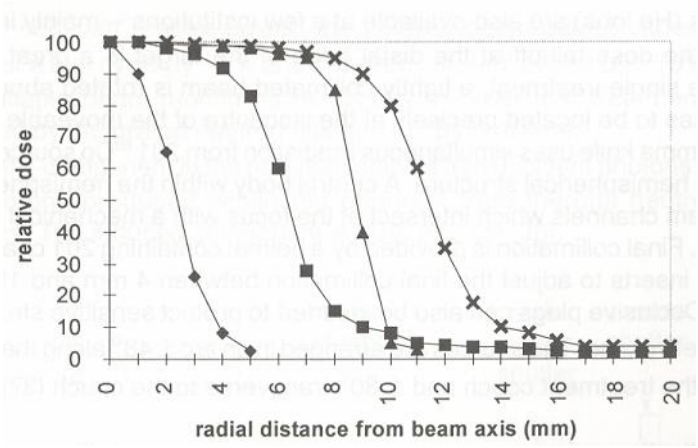

Figure 7 Transverse beam profiles of various stereotactic beams. Diamonds for a gamma knife with 4 mm collimator, squares for 6 MV X-ray knife with 12.5 mm collimator, triangles for 18 mm gamma knife and crosses for 6 MV X-ray knife with 22.5 mm collimator, from [7].

Figure 8 visually depicts the dose distributions with the various collimators in the gamma knife case.

Figure 8 Dose distributions represented with wooden models for the collimators used by a gamma knife [12].

When measuring the central axis dose, lateral electronic disequilibrium complicates the interpretation of the measurements since the detector has a finite size and the dose may vary significantly from the centre to its periphery. To minimise this effect the detector size should be smaller than the field size, which could be as small as 4 mm, shown in the above figures. A detector with small size or high spatial resolution is also necessary in order to resolve the large dose gradients at the penumbra. Both previous figures serve to demonstrate the magnitude of the task in hand for small field dosimetry.

To successfully address the dosimetry problems in small fields, various types of detectors have been used, namely ionisation chambers, films, thermoluminescent dosimeters (TLD) and silicon diodes. However, none of these provide an ideal solution [9]. Films, TLD and diodes have an energy depending response, with the former also suffering from statistical uncertainties in their measurements, which often make the results difficult to replicate. Diodes show angle dependence, whereas ionisation chambers are inadequate mainly because of their large size. This is highlighted in the work by Rise et al. [10] in the case of 6 MV beams. There, uncertainties of 2.5 % in the central axis dose of 12.5 mm wide fields were measured with a 3.5 mm wide ionisation chamber. The uncertainty in the beam profile measurements was up to 1 mm and the measurements were limited to 12.5 mm fields by the dosimeter's size. Thus, this detector would have been unable to resolve the dose distributions for the smaller collimator sizes shown in Figure 7. Finally, diodes and TLD do not inherently possess spatial resolution being single element devices, so either arrays have to be constructed by arranging individual devices side by side or a single device needs to be scanned across the field. The former solution has problems associated with the dead space between devices, as demonstrated in the original work of the Sheffield gamma knife group [11], whereas the latter is impractical when using a solid water helmet. Moreover, TLDs, like films, are not direct readout devices thus adding to the QA time burden, eventually restricting the patient throughput.

Thus, it would be of great benefit to the field of small field dosimetry, if a detector could be made that would be small enough to avoid problems with lateral electronic equilibrium, would have high spatial resolution sufficient to resolve the steep penumbras and direct read-out for real time measurements. This thesis will describe the results of a project[2] dedicated to deliver such a detector.

References

1. C J S Damerell, Veretex detectors: The state of the art and future prospects, RAL-P-95-008.
2. A study of GaAs detectors for tracking in the ATLAS experiment, S. Manolopoulos, RAL-TH-97-006.
3. J Kemmer, Nuclear Instruments and Methods A226 (1993) 44.
4. E Belau et al., Nuclear Instruments and Methods A214 (1983) 253.
5. F Hartman, Nuclear Instruments and Methods A549 (2005) 171.
6. The Physics of Radiation Therapy, F M Khan, Lippincott Williams & Wilknis, ISBN: 0-7817-3065-1.
7. A primer in applied radiation physics, F A Smith, World Scientific, ISBN: 981-02-3712-x.
8. Walter and Miller's Textbook of Radiotherapy Radiation Physics and Oncology, Livingstone, ISBN: 0443062013.
9. M Heydarian et al., Phys. Med. Biol., v. 41 (1996) 93-110.
10. R Rise et al., Phys. Med. Biol., v. 32, no. 9 (1987) 1087-1099.
11. L Walton et al., The British Journal of Radiology, v. 60 (1987) 897-906.
12. http://www.shef.ac.uk/~ns/web/WhatIsGammaKnife.htm , web page of the "Sheffield's Gamma Knife centre, STH N HS Trust".

[2] Project DOSI, "A High Resolution Dosimeter for Small Field Dosimetry " funded by the Department of Health (HTD122) and PPARC (PPA/I/S/2002/00662/2).

2 Experimental Set-up

2.1 The radiation source

A megavoltage linear accelerator (MV LINAC) was used as the source of X-rays for all hospital measurements. The main components of a LINAC are [1, 2]:

- The injection system, usually an electrostatic accelerator ("electron gun") that consists of the electron source and electrodes. The former is a tungsten filament from which electrons are emitted thermionicaly and the latter are used for focus and the initial electron acceleration to typical energy values 50-100 keV.
- The radio-frequency system that comprises of the master r/f oscillator and microwave power generator, like a klystron, which provide the microwave power via the wave guide for the main acceleration and are also responsible for the grouping of electrons in "bunches" making the LINAC a pulsed source.
- The beam transport system responsible for the main electron acceleration and includes the waveguide for the transfer of the microwave power, the accelerator tube and the magnets for steering and focusing purposes.
- The treatment head, where the final focusing takes place, as well as the production of X-rays by bremsstrahlung following the electron absorption by a metallic target, e.g. tungsten. Additional components therein are flattening filters, primary and secondary collimators, responsible for the final shape of the X-ray beam, as well as beam monitoring devices, for dose, dose rate and field symmetry measurements and adjustments.
- The supporting systems, like vacuum and air pressure pumps, gas system, water cooling system, shielding for radiation protection equipment.

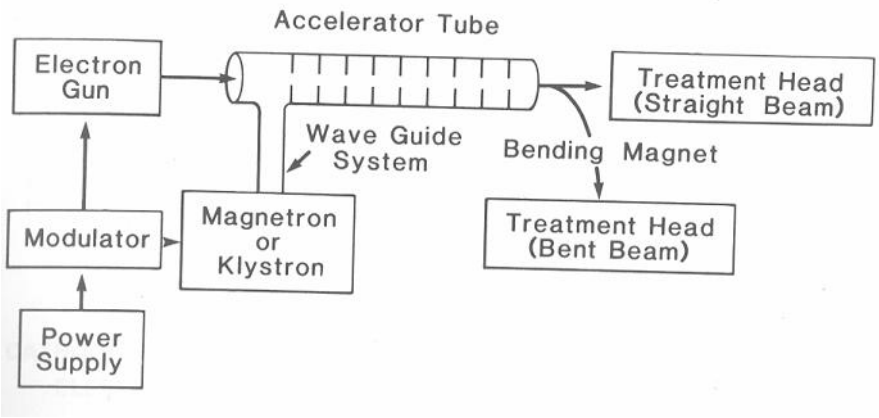

Figure 9 Block diagram of a typical medical LINAC, from [2].

Of particular importance for the modern radiotherapy modalities is a special set of collimators the multileaf collimators (MLC). They are located at the end of the treatment head as an add-on component after the secondary collimators, or sometimes replacing them altogether. MLCs are series of opposing leaves, typically 60 leave pairs, each leave individually controlled by a computer. They are used to provide irregular field shapes and are one of the key enabling technologies behind IMRT. They are made of tungsten alloys and have a thickness along the beam direction ranging from 6 to 7.5 cm, depending on the accelerator design, but in anyway

sufficient to provide less than 2% transmission. A "tongue & groove" design is used to minimise leakage between adjacent leaves, typically less than 3%. Finally, the leaves have a curved shaped ends to avoid beam hardening and for sharp penumbras.

Figure 10 Picture of a multileaf collimator[3].

All hospital measurements described in the next chapters were taken at the Weston Park Hospital in Sheffield using a Varian 2100 CLINAC® linear accelerator equipped with multileaf collimators (MLC), see Figure 11. The detector was sandwiched between slabs of a solid water phantom to allow for full scatter conditions. The surface-to-source distance (SSD) was 100 cm and the phantom thickness varied, but it was always enough to provide charge particle electronic equilibrium conditions, e.g. more than 1.5 cm for 6 MV X-rays. The lateral distance of the detector to the phantom's edge was more than 3cm, once more guaranteeing with (lateral) electronic equilibrium.

Figure 11 The linear accelerator used in the hospital measurements.

[3] courtesy of Varian Medical Systems, http://www.varian.com

2.2 Standard dosimeters

Various dosimeters from the hospital standards have been used as reference and also for "cross checking" purposes throughout the tests.

2.2.1 Thimble chamber

This is a small "air-wall" ionisation chamber (typical volume 0.6 cm^3) used for absolute X-ray dosimetry. Shown in Figure 12, it consists of an aluminium central electrode (wire) with a typical diameter of 1 mm and a length of around 20 mm, surrounded by a graphite wall (cap) of 7 x 25 mm (diameter x length). Developed in the early 1970's by Aird and Farmer [6] as an improvement of the original Farmer chamber that was used as a secondary standard in photon dosimetry it shows a characteristic response that does not vary significantly from one instrument to another. By incorporating the Bragg-Gray cavity theory that assumes:

- the presence of the cavity does not perturb the charge particle field, i.e. their range is greater than the cavity dimensions and
- the dose within the cavity is entirely due to the charged particles, i.e. they are neither generated nor absorbed in the gas volume but start and stop in the wall material.

One can determine the dose in the wall material (D_g) from the measurement of the ionisation inside the cavity. This is done by the simple formula:

$$\frac{D_w}{D_g} = \frac{{}_mS_w}{{}_mS_g} \Rightarrow D_w = \left(\frac{Q\ w}{m\ e}\right)_g \left(\frac{{}_mS_w}{{}_mS_g}\right) \qquad \textbf{Eq. 1}$$

where Q is the charge liberated in the gas, m is the mass of the gas, w the mean energy to create an electron-hole pair in the gas, e the electron charge and ${}_mS$ the mass collision stopping power for the secondary charged particles for the wall (w) and gas (g) materials. As such, "B-G" does not require the presence of charged particle equilibrium for the determination of dose. However, the wall thickness usually varies and a "build-up cap" maybe added (as shown in the figure) depending on the photon energy range to provide charge particle equilibrium. For completeness, a number of corrections are commonly added to the above formula for the calculation of dose, to account for temperature, pressure and ion recombination effects.

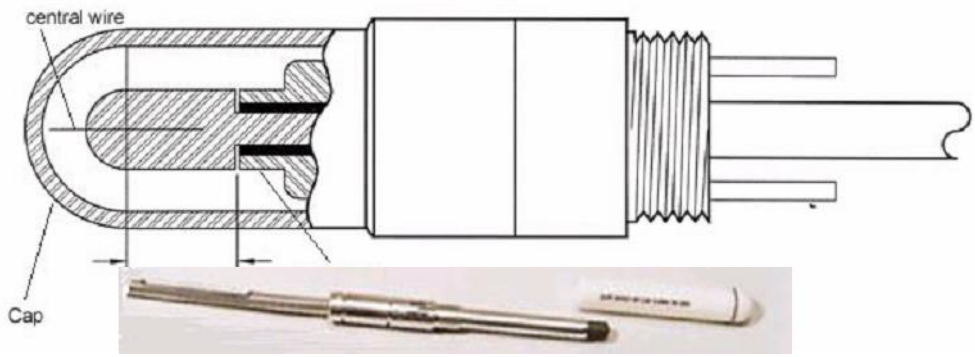

Figure 12 Thimble ionisation chamber.

2.2.2 Film

Radiographic film is usually employed for relative dosimetry. It consists of an emulsion of silver bromide (AgBr) grains dispersed in a gelatine binder that acts as the active medium and is

deposited on either side of a plastic base for support and encapsulated by a thin plastic coating. As a result of the energy deposition that follows an X-ray exposure the AgBr grains are converted to elemental silver close to the interaction point. Thus a "latent" image is created, which is subsequently amplified by the chemical reactions in the development stage that result in a measurable reduction of the optical transparency, i.e. an increase of the optical density. This can then be measured by means of a densitometer and assuming a linear response (true when a small fraction of AgBr is converted) it will be proportional to the absorbed dose [1].

2.3 The detector

The detector is made on high resistivity (1-10 kO cm) 300 µm thick n-type silicon, on which a linear array of p-type diodes are fabricated by ion implantation. The diode pitch is 250 µm to provide sufficient resolving power for sub-millimetre resolution. A multi-guard ring structure surrounds the pixel array in order to minimise the surface component of the leakage current by drawing away the excess current from the edges and also to define the active volume [3], see Figure 13.

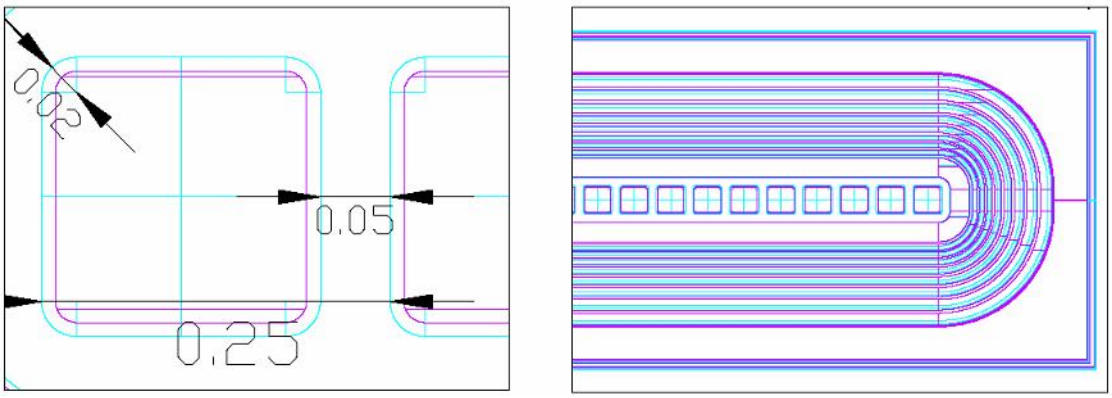

Figure 13 Left-hand side, a drawing detail of a detector element (pixel) and its dimensions with units in millimetres. On the right, a drawing of the end of detector array and its guard ring structure.

A prototype dosimeter is shown in Figure 14. From left to right of the picture one sees the detector, the rectangular dark box on the top of the green coloured printed circuit board (PCB), followed by the front end readout electronic integrated circuit (ROIC), not visible being placed underneath the silver protection cover. The distance of the detector to ROIC allows for the appropriate layout of tracks but mostly acts as a precautionary against radiation damage of the electronics by accidental exposure to the MV X-rays. Also shown in the picture are the various electronic components for the ROIC control and data acquisition with most significant among them the 14bit ADC converter and the fully programmable gate array (FPGA) the black square with white label on right hand side. A more detailed description of dosimeter is given in the following section.

Figure 14 Picture of the 128-channel prototype detector and associated electronics.

2.4 The readout electronics

The XDAS[4] DAQ system is used for the detector read-out [4]. This consists of a 128 channel preamplifier ROIC, the X2CHIP[5]. The preamplifiers work in charge integrating mode with a variable capacitance on the feedback loop for gain and dynamic range control [5] that is externally discharged by means of a FET, see Figure 15. A main feature is the dual sample and hold (S&H) circuitry for every channel, i.e. the capacitance C1 and C2. This allows the chip to be active during read-out, keeping the dead time to a minimum (less than 1 μs, defined by the width of the RESET pulse)[6]. It also allows for true correlated double sampling (CDS) a technique for fixed pattern noise reduction [5]. For each channel the output of the integrating amplifier is sampled at the beginning and at the end of the integration period on a different pair of capacitors, e.g. C1A and C1B. At the end of the integration period the two stored voltages of C1A, C1B are read via a multiplexer to a differential amplifier, thus the final analogue output is the voltage difference that corresponds to the integrated charge generated at the detector during the integration period. Digitisation takes place on board by a 14-bit ADC and the read-out chain is completed by a fully programmable gate array (FPGA). This is used for local memory storage and simple, "on the fly", image processing, like background subtraction, gain normalisation and signal averaging. The digital data are then finally sent to the computer via a shielded SCSI cable for storage and further (off line) processing. The XDAS DAQ system allows for integration times between 10 μsec to 50 msec with the ability to extend the latter to 10 sec by adding up to 512 frames at the on-board memory (digital signal averaging). The maximum read-out rate is 5 Mb/sec when read by a dedicated PCI card and up to 63 boards can be daisy-chained to form a single system. The maximum charge ("well capacity") that can be stored per channel is 15 pC. Finally, it should be noted that XDAS can be used either in asynchronous or synchronous readout mode being triggered either internally or by an external pulse, e.g. from the LINAC.

[4] Provided by ETL Ltd., Ruislip, UK
[5] Designed by CCLRC, RAL, Didcot, UK
[6] The system's dead time is around 110 μs defined by the ADC speed.

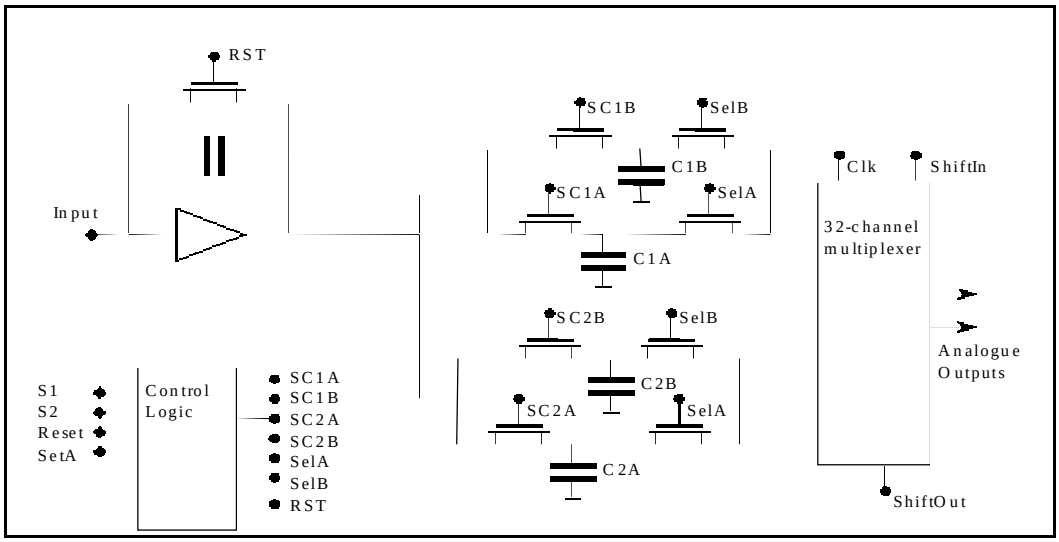

Figure 15 Functional diagram of a single channel of the XCHIP readout chip.

References

1. A primer in applied radiation physics, F A Smith, World Scientific.
2. The physics of radiation therapy, F M Khan, Williams&Wilkins publishing.
3. Semiconductor radiation detectors device physics, G. Lutz, Springer-Verlag Berlin and Heidelberg GmbH.
4. XDAS User manual, Electron Tubes Ldt. http://www.electrontubes.com/
5. The Art of electronics, P. Horowitz and W. Hill, Cambridge University Press.
6. E. Aird and F. Farmer, Phys. Med. Bio. v. 17, No. 2 (1972) 169-174.

3 Measurements

3.1 Electrical tests

Standard electrical measurements for the detector characterisation should precede any tests with radiation, as indicative for the operating conditions of the device. They could also provide helpful data that assist the analysis of the detector response to radiation, for example by providing insight to the expected noise levels thus allowing for a back-of-the-envelope determination of the energy resolution. In the case of semiconductor detectors the most fundamental of these measurements are those of the current and capacitance as a function of applied voltage, called current-voltage (I-V) and capacitance-voltage (C-V) characteristics respectively.

3.1.1 I-V characteristics

Almost all semiconductor detectors are based on a p-n diode configuration, especially those that work in the photocurrent mode. The ideal current-voltage characteristic for a diode is given by the famous Shockley equation, commonly known as the "diode law" [13]:

$$J = J_o\left(e^{qV/kT} - 1\right) \qquad \textbf{Eq. 2}$$

where J_o is the leakage current density, q the charge of the electron, V the applied voltage, k the Boltzmann constant and T is the temperature of the device. An example of an I-V curve is shown in Figure 16. The ideal diode law holds for abrupt junctions, at low injection levels and when no generation current is present. Under these conditions, the leakage current is given by:

$$J_o = \frac{qD_p p_{no}}{L_p} + \frac{qD_n n_{po}}{L_n} \qquad \textbf{Eq. 3}$$

where D_p (D_n) the diffusion coefficient for holes (electrons), p_{no} (n_{po}) the concentration of holes (electrons) in the n (p) region under equilibrium conditions and L_p (L_n) the diffusion length for holes (electrons). The leakage current depends strongly on temperature and varies as exp($-E_g/kT$), where E_g is the bandgap.

When, minority carrier generation-recombination is important, as in the case of silicon detectors, the above equation gets modified as:

$$J_o = q\sqrt{\frac{D_p}{\tau_p}}\frac{n_i^2}{N_D} + \frac{qn_iW}{\tau_e} \qquad \textbf{Eq. 4}$$

where τ_p is the diffusion lifetime of holes, τ_e the effective lifetime of the minority carriers in the depletion region, n_i intrinsic carrier concentration, N_D the donor concentration and W the width of the depletion region. The first term is the diffusion part of the current, whereas the second term describes generation-recombination inside the depletion region. It also assumes carrier depletion predominantly in the n-side of the junction as is the case when $p_{po} >> n_{no}$, i.e. when the p-side is more heavily doped. Following the application of reverse bias, the leakage current in the generation-recombination case does not saturate, but increases with increasing voltage as a function of $V^{1/2}$ reflecting its dependence of the width of the depletion region, which also grows like $V^{1/2}$. Finally, there are other factors that contribute to the leakage current like the quality of the metal contacts, the presence of in the forbidden energy zone (bandgap) and surface effects. These all are more difficult to describe as they depend largely on manufacturing process, like surface passivation etc.

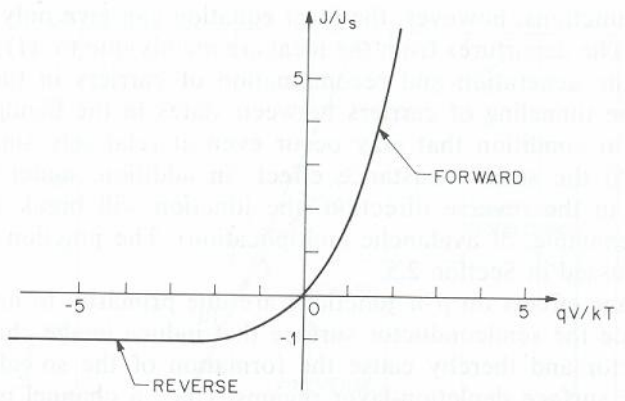

Figure 16 The current-voltage characteristic curve for an ideal diode from [13].

3.1.2 C-V characteristic

The capacitance of a n one-sided abrupt junctio n is given by [13]:

$$C = \frac{\varepsilon_s}{\sqrt{2L_D}} \left(\beta V_{bi} \pm \beta V - 2\right)^{-1/2} \qquad \textbf{Eq. 5}$$

where C is the capacitance per unit area (F/m^2), e_s the semicon ductor permittivity, L_D the Debye length, ß is a parameter that depen ds on the temperature, V_{bi} the built-in potential, V the applied voltage and the ± sign applies to conditions of reverse and forward bias respectively. Reverse biasing the diode increases the depletion region , consequently decreases the capacitance ($C \propto A/L$) with the minimu m given at f ull depletion.

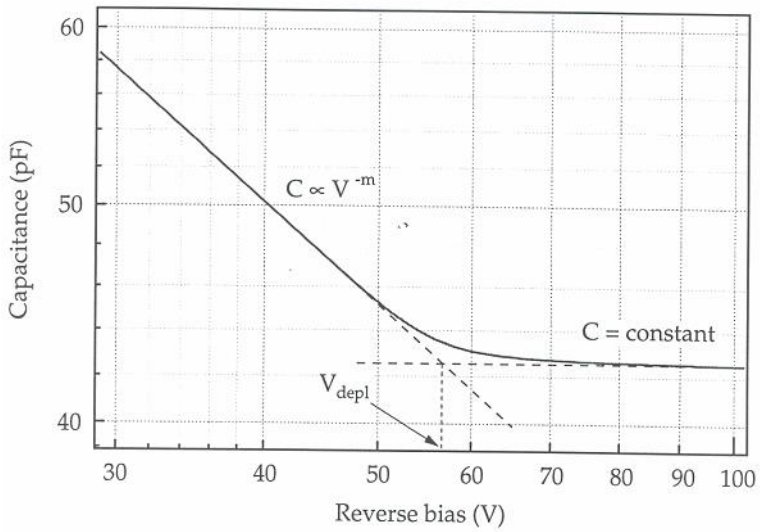

Figure 17 C-V charact eristic curve for a d iode detect or from [14].

It is clear from the ab ove e quation that by plotting $1/C^2$ versus V one should obtain a straight line:

$$\frac{1}{C^2} = \frac{2L_D^2}{\varepsilon_s^2} \left(\beta V_{bi} \pm \beta V - 2\right) \qquad \text{Eq. 6}$$

the slope of which will determine the impurity concentration because of the Debye dependence, $L_D \propto \sqrt{N}$, whilst the ordinate's intercept will depend on the built-in potential for a given temperature.

3.2 Dosimetric measurements

The detector developed in this project was aimed as a dosimeter for stereotactic radiosurgery (SRS). The main quantities of interest in SRS dosimetry are: a) central axis dose distribution, e.g. percentage depth dose curves, b) off axis ratios, i.e. cross-beam profiles and c) dose output factors [1]. However, access to Weston Park Hospital's gamma knife was not possible for the duration of this project due to patients' demand for the facility, thus we had to resort for the purpose of the measurements to the use of a MV LINAC of the type shown in the previous chapter. Nonetheless, the said quantities are the basic beam data needed as input to the treatment planning software in all teletherapy modalities, either in megavoltage radiotherapy or stereotactic radiosurgery, thus crucial in defining the overall accuracy of the treatment [16]. Therefore, these sets of data will be acquired during acceptance testing and commissioning of a new LINAC and continuously monitored by periodic QA checks throughout the "clinical" lifetime of the machine. Hence, any new detector that is to be of use to the medical physicist in aspects of dosimetry for radiotherapy should be firstly "benchmarked" against these most fundamental of quantities.

3.2.1 Percentage Depth Dose

The percentage depth dose (PDD) curve shows the central axis dose variation with tissue depth. It is measured by placing small volume dosimeters (like ionisation chambers, TLDs etc.) at various depths of water or water equivalent phantoms (PMA, solid water etc.) on the central beam axis. PDD is defined as:

$$PDD(d, A, f, E) = 100 * \frac{D_Q}{D_p} \qquad \textbf{Eq. 7}$$

where Dq and Dp is the dose in the points Q and P (the point of maximum dose), shown in Figure 18. Apart from its explicit dependence of depth, PDD also varies with field size (A), source to surface distance (f) and beam energy (E).

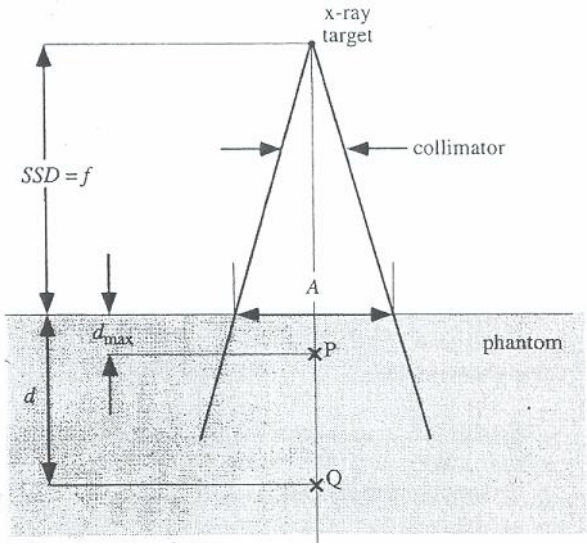

Figure 18 Schematic drawing of the parameters that define PDD, from [16]

Typical PDD curves in MV photon beams, show an initial rise with depth up to a maximum dose, the build-up region, followed by an almost exponential decay, see Figure 19. The former is due to the range of the secondary electrons, whereas the latter follows the attenuation of the primary photons with depth. PDD increases with field size because of an increase in the relative scatter contribution. Likewise, it increases with increased SSD due to the inverse square law dependence

of dose rate with distance from the source. At first sight, this may appear counterintuitive, as an increase of SSD should produce a decrease in the photon flux according to the inverse square law. However, it is the shape of the "$1/R^2$" curve, which is steeper for small distances and falls less rapidly for larger distances that determines the SSD dependence of the PDD curve. The latter being a relative dose measurement between one point and a reference one (usually d_{max}) reflects relative changes in dose, showing an increase with increased distance, where the dose "fall off" due to "$1/R^2$" is more gradual. Finally, PDD increases with beam energy, see Figure 19. Also worthy of noticing in this figure is the increase of d_{max} with increasing energy, as a consequence of increased forward scatter contribution and electron range.

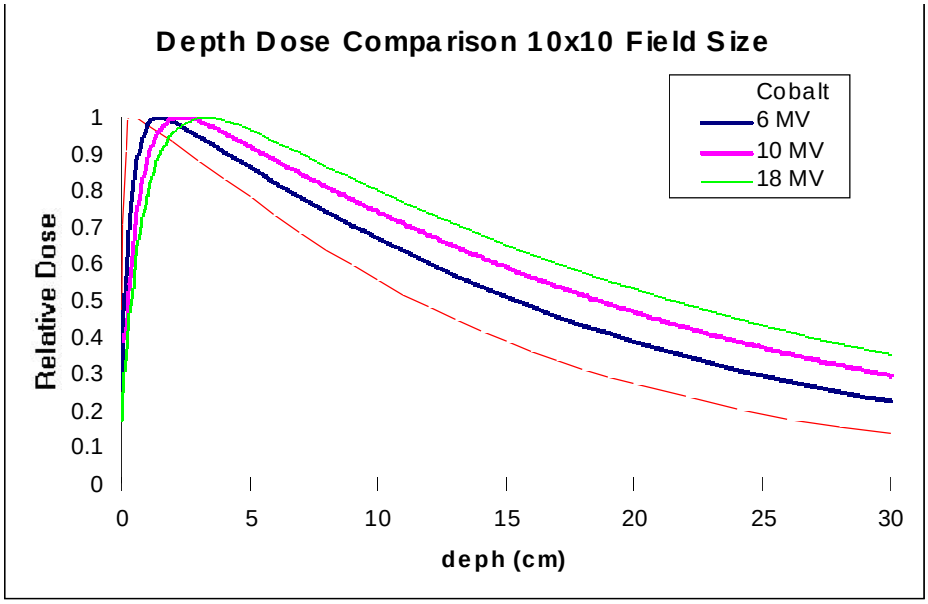

Figure 19 PDD curves in water for a 10x10 cm^2 field at a SSD of 100 cm for various LINAC photon energies, from [17].

3.2.2 Beam Profile

Beam profiles are essential as are used, in conjunction with PDDs, for the calculation of isodose distributions. They represent dose measurements across the beam that is perpendicular to the beam axis, at a certain depth. Typical profiles for MV beams consist of two regions, the umbra (central part) and the penumbra (edges), as shown in Figure 21, for a LINAC similar to the one used in this project. The umbra region extends to within 10 to 15 mm from the geometric field edges of the beam. The latter usually defined at the 50% dose level points on the profile. However, the area of most interest especially to small field dosimetry is the penumbra region due to the steep dose gradients encountered there. It is a combination of two penumbrae types: the geometric penumbra and the transmission one. The former depends on the size of the source, the collimators and the SSD and can be calculated by the following equation, based on the parameters shown in Figure 20.

$$P = S\left(\frac{SSD - L}{L}\right) \qquad \textbf{Eq. 8}$$

where P is the width of the penumbra region, S the source size, SSD the source to surface distance and L the source to beam defining collimator distance.

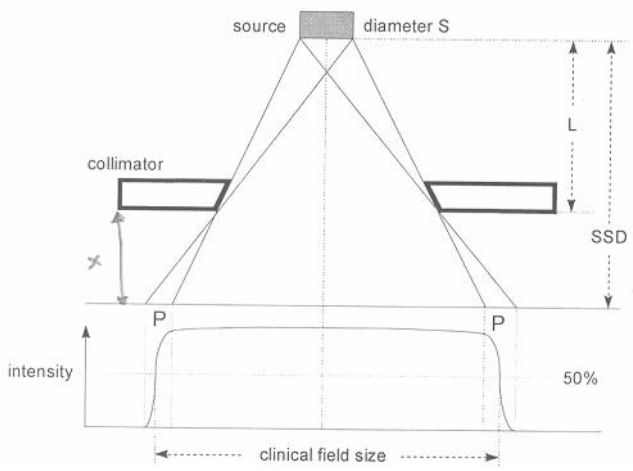

Figure 20 Geometric penumbra formation, from [1].

The transmission penumbra is due to unavoidable radiation leakage through the collimator edges, as well as scatter contribution. To minimise its effect, both primary and secondary collimators have an oblique shape that attempts to match the beam's divergence. Nonetheless, transmission penumbra cannot be completely removed for all field sizes.

Consequently, the dose distribution at the edges of the beam profile has a sigmoid shape and extends under the collimators. It is because of this rapid fall of the dose in the penumbra that detectors with very good spatial resolution are required for profile measurements. For example, it has been shown that in SRS detector sizes down to 3.5 mm in diameter are needed in order to successfully measure beam profiles in the range of 12.5 mm and onwards [18]. This is sufficient for the larger of the collimators employed in a gamma knife, but does not meet the more stringent demands imposed by the smaller ones, with diameters as low as 4 mm [19]. Once again, the accurate determination of the dose at the penumbra region of the beam is of crucial importance, as it will influence the accuracy of the dose calculation by the treatment planning system.

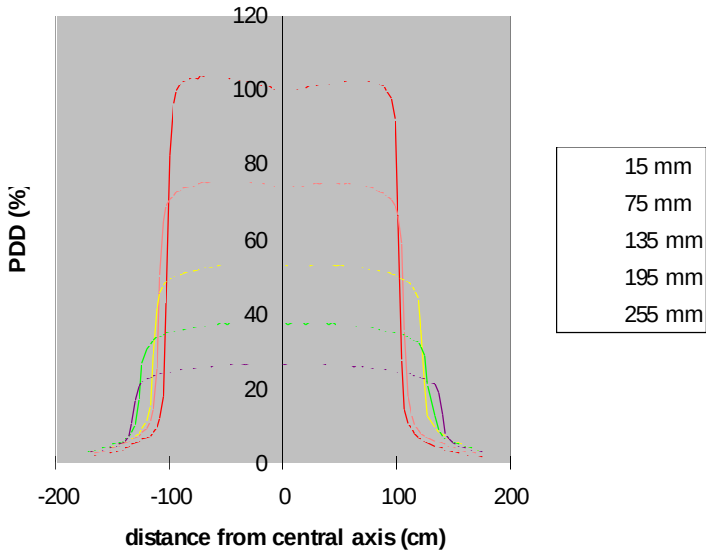

Figure 21 Example of beam profile curves at various depths. Beam energy 6 MV, field size 10 x 10 cm^2, data taken with a VARIAN 2100 LINAC, from [17].

3.2.3 Dose Field Factors

The LINAC dose monitoring system measures dose in monitor units (MU) with the relation between MU and dose units being machine dependent. In most cases 1 MU is been chosen to correspond to 1 cGy delivered at d_{max} in water, for a 10x10 cm^2 field and at 100 cm SSD. This correspondence is no longer valid for other field sizes, being smaller for smaller fields and vice versa. However, since MU's are used to monitor the patient dose delivered during treatment the effect of field size on dose rate (in cGy/MU) must be accounted for. Output factor, otherwise known as collimator scatter factor (S_c) is one form of dose field factors that account for the variation of dose rate (in cGy/ MU) at a point (e.g. d_{max}) with field size. It is defined as the ratio of dose at a point (e.g. d_{max}) in air for a given field (A) to that of a reference field (usually 10x10 cm^2) [1]:

$$S_c = \frac{D_p^{air}(A)}{D_p^{air}(10x10)} \qquad \textbf{Eq. 9}$$

It may be measured with an ionisation chamber with a build cup with a typical set-up as shown in the A) below .

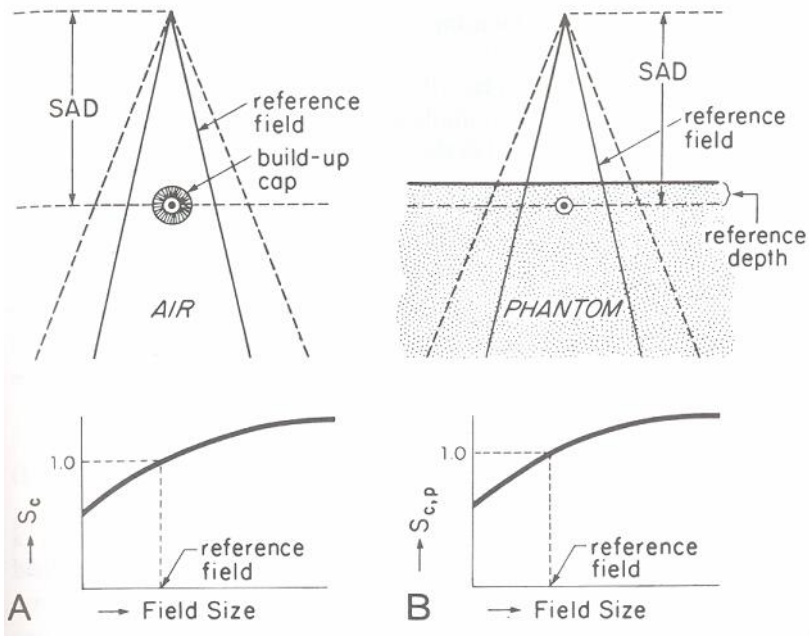

Figure 22 Experimental arrangements for the measurement of collimator (figure A) and phantom (B) scatter factors [1].

For completeness, the phantom scatter factor (S_p) also shown in Figure 22 accounts for the scatter contribution due to the presence of the phantom material. Finally, the total scatter factor is the combination of both these factors given by:

$$S_{c,p}(r) = S_p(r) * S_c(r) \qquad \textbf{Eq. 10}$$

where r is the distance to the source.

References

13. Physics of Semiconductor Devices, S M Sze, Wiley & Sons pub., ISBN: 0-471-05661-8.
14. Defect Kinetics in Silicon Detector Material for applications at the LHC, B M MacEvoy, RAL-TH-97-003.
15. The Physics of Radiation Therapy, F M Khan, Lippincott Williams & Wilknis, ISBN: 0-7817-3065-1.
16. The Modern Technology of Radiation Oncology, Jacob Van Dyke, Medical Physics Publishing (Wisconsin) 1999, ISBN 0-944838-38-3.
17. I. Rosenberg, MSc lectures.
18. R Rise et al., Phys. Med. Biol., v. 32, no. 9 (1987) 1087-1099.
19. L. Walton et al., The British Journal of Radiology, v. 60 (1987) 897-906.
20. A primer in applied radiation physics, F A Smith, World Scientific.

4 Analysis

This chapter describes the experimental work undertaken in this project, specifically the details of the measurements described in the previous chapter and the data analysis.

4.1 Electrical Measurements

The general principles behind the I-V and C-V characteristics were given in the previous chapter. A brief description of the experimental set-up used for their measurement will be given at the beginning of the corresponding section. Further measurements of "quantities of interest", like linearity, will be described in following sections (4.1.3) together with its set-up. Finally, there is a calibration and cross-talk section (4.1.4) that however does not require a special set-up but are rather a by-product of the linearity measurements.

4.1.1 I-V characteristics

A Keithley© 487 picoammeter-voltage source was used. This measures the current for a given value of the applied voltage. The instrument is remotely controlled by a PC via a GPIB (IEEE) interface and LabView© software. The user defines the voltage range by indicating the starting and finishing voltage values and step. The "settling" time, i.e. the time between the application of the voltage and the current measurement is also user defined, which in our case was set to 1 s. Each current recording is the average of a predefined number of measurements, here ten, at a constant voltage. A threshold value is used for the current, here 1 µA, to avoid device damage due to excessive current flow, for example following breakdown. Finally, all measurements were done in a dark box to avoid systematic errors due to photocurrent, as silicon is responsive to visible light. A schematic drawing of the set-up can be seen in the next figure.

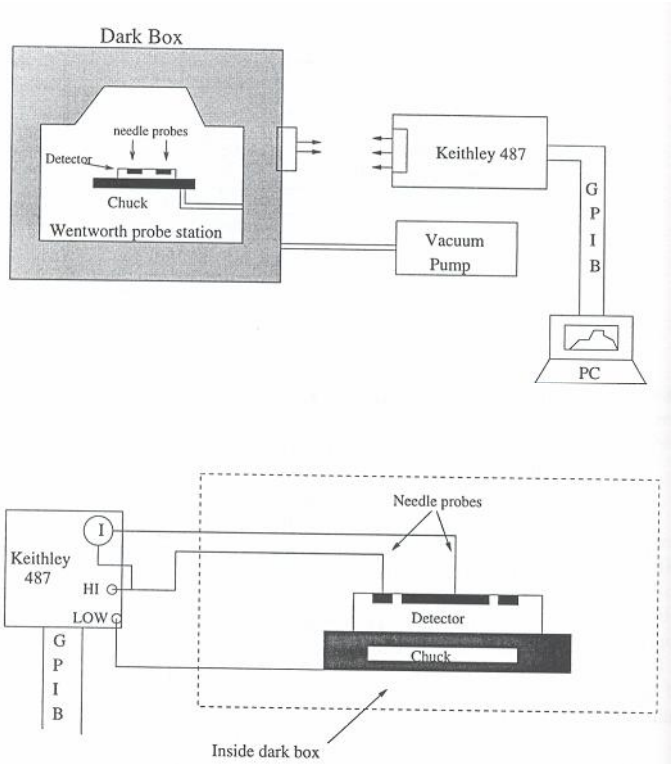

Figure 23 Schematic for the I-V measuring set-up and detail of the measurements' configuration connection.

A typical example of the characteristic curve for a diode in one of our detectors is shown in the following figure, taken at 20 °C.

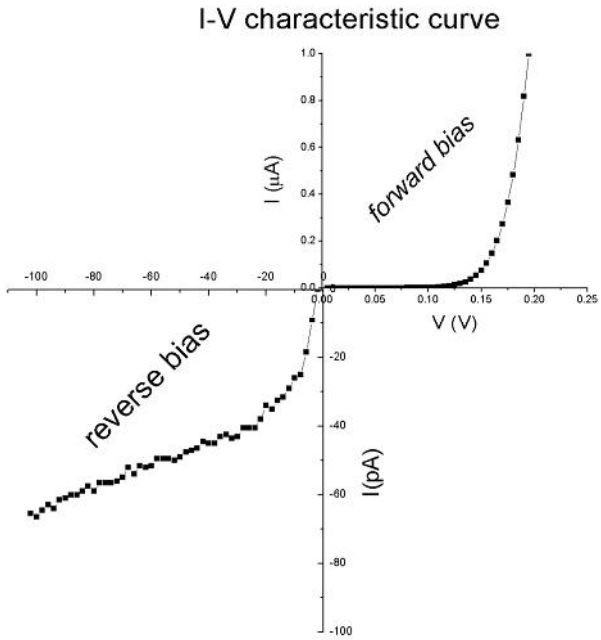

Figure 24 Example of an I-V curve for a typical diode in our detectors measured at 20 °C.

The two branches of the I-V curve, forward and reverse, are evident as expected from the standard diode theory. The forward branch shows an exponential increase of the current with bias, in accordance with the Schokley's equation for the ideal diode. On the contrary, the current at reverse bias stays approximately constant with bias, with a slight increase due to surface (passivation etc.) and volume (depletion etc.) effects, as explained in the previous chapter. Worthy of notice is the almost six orders of magnitude difference between the two currents.

To further check that this was indeed a typical behaviour for a detector, the following figure shows the reverse I-V branches for a number of diodes on the same detector. Most measurements are within 1 pA with the biggest variation encountered being around 20 pA.

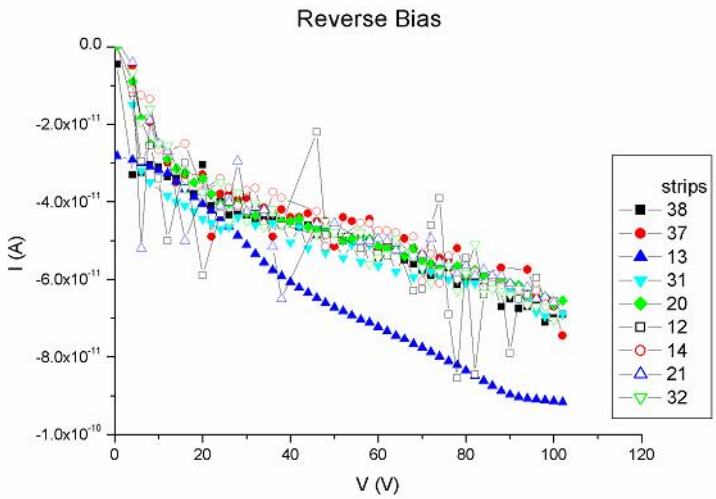

Figure 25 I-V curves for a number of diodes of the same detector.

Finally, the systematic variation in leakage currents between different detectors was tested. The following figure shows the current distributions for all hundred-and-twenty-eight (128) diodes in a detector at a constant voltage, for detectors of the same silicon wafer in different stages of the fabrication process. This is of particular interest as it provides the manufacturer with crucial feedback for the fabrication process. For our benefits, it provides us with an insight of the effects that the various fabrication steps have on leakage current as well as their relative magnitude. Thus, the mean of the leakage current at the depletion voltage (see next section for the derivation of the latter) for an unpassivated detector was around 0.7 nA, with less than 0.2 nA variation between detectors. This increased to around 4 nA for a fully processed detector, but with bigger variations between detectors of the order of 2nA, to the limits of our statistics. Nonetheless, this is still within the acceptance limits of the manufacturer and the specifications of this project. Finally, similar values were found for detectors of different wafers with the spread in values not exceeding that of a few nA (typical 3 nA). In all the above the voltage was measured with a 5 digit accuracy (10^{-5}) with a similar error for the current readings [1].

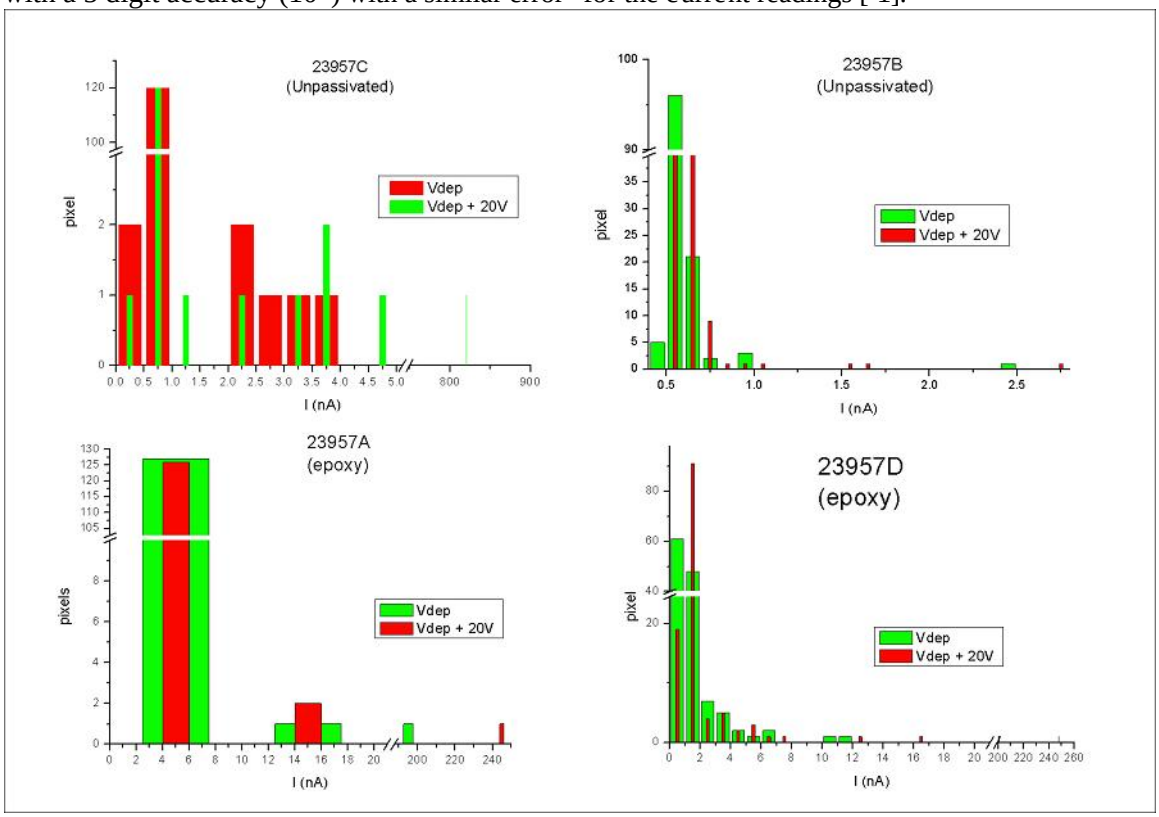

Figure 26 Currents distribution of all diodes at fixed voltage for different detectors of the same silicon wafer.

4.1.2 C-V characteristic

For the measurement of the C-V characteristic curve a Hewlett-Packard© 4274A multi-frequency LCR meter was used together with a Keithley© 487 for bias supply. The set-up is identical to the one shown in Figure 23 with the LCR being inserted between the Keithely 487 and the detector, both under the control of LabView© software. Once again, the user defined the range and step of the voltage measurements, the settling time, as well as the number of samples for the capacitance reading at each voltage. A frequency of 100 kHz was selected as appropriate for silicon detectors. Finally, the user has to select between two models, a parallel and a series one, see [1]. This depends on conditions regarding the relative significance of the impedance components of a

diode, represented with the model shown in Figure 27. There, C and R_p are the capacitance and resistance of the depleted region, whereas R_s represents the series resistance of the undepleted part. There are two measurement conditions, one described by the series model ($R_p >> 1/?C$) and the other by the parallel ($R_s << 1/?C$).

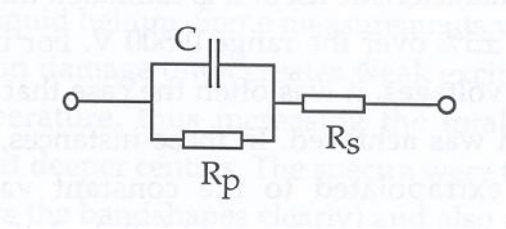

Figure 27 Circuit model of a diode for the interest of the CV measurements

1) Series model. Typical values of R_p for detector graded, i.e. high resistivity silicon, are ~ 10MΩ. The diode capacitance was 30 pF, thus at 100 kHz the capacitive impedance was $1/?C \cong$ 50 kΩ. Therefore, the condition $R_p >> 1/?C$ of this model is satisfied.

2) Parallel model. Once again based on typical values for the resistivity of detector graded silicon (ρ ~ 10 kΩ cm) and the diode dimensions ($A \cong 6\ 10^4$ cm^2, L = 300 μm) one calculates the resistance of the undepleted part as $R_s = \rho\ (L/A) \cong 5$ mΩ $<< 1/?C$, so this condition is also satisfied.

As either model was appropriate in our case, we chose for our measurements the one most commonly encountered in the literature, i.e. the series model. An example of a C-V characteristic for a typical diode in our detectors is shown in the Figure 28.

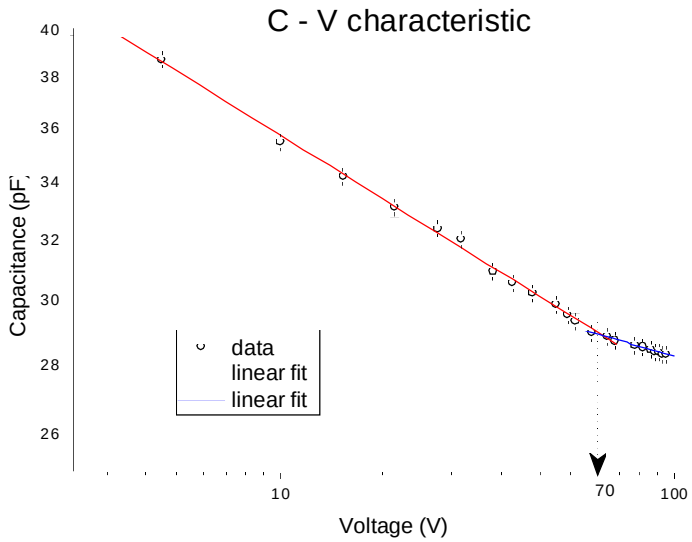

Figure 28 C-V measurement for a typical diode.

From the figure above one can derive the depletion voltage, in accordance with what was described in the previous chapter, from the intercept of the two linear parts of the curve. This was found to be around 70 V. The error in the capacitance measurement was 0.1% across the range whereas the voltage uncertainty was as given in the previous section (10^{-5}) [1]. The error in the derived value for the depletion voltage is around 1V mainly by deciding the point of intercept for the two linear parts of the curve.

4.1.3 Linearity tests

A linear response across the dynamic range is of paramount importance for any dosimeter. When the response is nonlinear one has to make assumptions, as in the case of films, that the measurements are restricted to the linear part of the response or energy dependent correction factors have to be employed, each of which has its own uncertainties. The linearity in the response of silicon or other semiconductor detectors to radiation is well documented, so what was of interest here was to check the response of the read-out electronics, as this will consequently define the system's linearity. To that extent, a fixed amount voltage, represented by a square pulse, was applied to the input of the preamplifiers (XCHIP) and the output response of the ADC was recorded. This was done by connecting a pulse generator in series with an external capacitor of known value (10 pF), which was in turn connected to the preamplifier input. A typical plot for the response is presented in Figure 29.

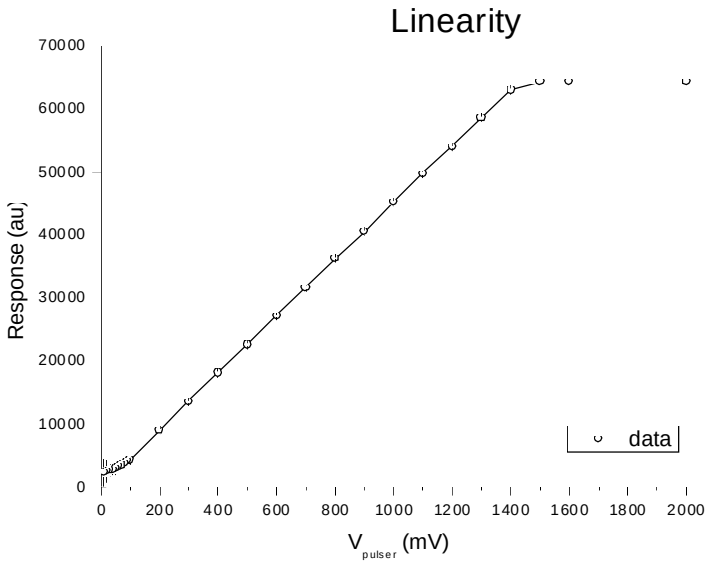

Figure 29 Linearity plot for the response of the DAQ system (XDAS).

The response is in terms of ADC units (ADU) whereas the voltage values are as dialled in the pulse generator (3-digit accuracy). As is evident in the figure the readout electronics have a linear response across the dynamic range (65000 ADU). The apparent deviation from linearity at low voltage values is mostly due to the noise of the electronics, which becomes more important for low signals. This is further evident in the statistical error of the response measurement, which increases with decreasing signal height and becomes significant for signals approaching the pedestal levels, typical around 1200 ADU.

4.1.4 Calibration and cross-talk

It is a straightforward process to convert the linearity to a calibration plot since the input capacitance is known and measured to be 10.35 ± 0.01 pF. Thus, one can calculate the injected charge to the preamplifier input as the product of the input capacitance and the applied voltage (Q = C * V), therefore obtaining a relationship between system response in ADC units and input charge, i.e. a calibration curve.

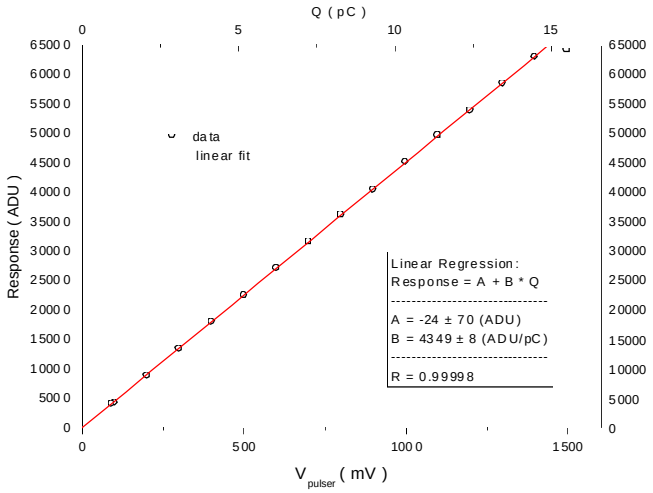

Figure 30 Calibration curve for the XDAS DAQ system.

By fitting on the linear part of the curve, one obtains the calibration constants, as shown in Figure 30. Finally, the data in the calibration curve are in agreement with what is expected based on the specifications provided by the manufacturer, i.e. the saturation charge is in agreement with the "well capacity" of each channel of 15 pC [3].

A finally quantity of interest is the "cross talk". This is defined as the response of the neighbour channels for a stimulus on the input of the intermediate (central) channel. Its importance lies on the fact that it will be a contribution to the system spatial resolution from the electronics perspective, as any charge created by the radiation on a detector channel will "leak" to the neighbouring ones, thus creating a signal response, where none should be expected. To evaluate the level of cross talk in our system, we measured the average response of the adjacent neighbours either side of a stimulated channel as a function of the size of the central channel stimulus, shown in the next figure.

The level of cross talk can be quantified by calculating the ratio of the neighbour response to that of the central channel at a given voltage. Thus, for input signals close to but before saturation, e.g. for an input voltage of 1400 mV (corresponding to 14.5 pC of injected charge) this is found as 45 ADU / 62874 ADU $\approx 7\ 10^{-4}$. Therefore, we conclude the maximum cross talk regarding the read out electronics is a less than 10^{-3} effect.

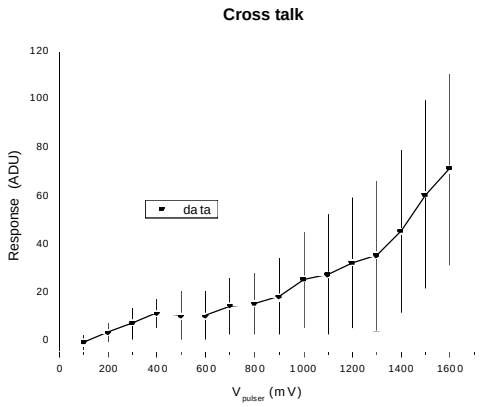

Figure 31 Cross talk for the XDAS DAQ system.

4.2 Dosimetric measurements

These are the most important of the measurements as the primary function of our detector is relative dosimetry for radiotherapy modalities. Therefore, its ability as a dosimeter will be evaluated on its performance in measuring the dosimetric quantities of interest, presented in the previous chapter.

4.2.1 Percentage Depth Dose

The variation of the central (beam) axis dose with depth in water (tissue) was measured by means of a phantom made by solid water. The detector was positioned on the icocentre with the aid of the LINAC's optical alignment tools (lasers) and individual slabs of solid water were added on top to provide different depths. The SSD was kept constant at 100 cm as was the field size of 10 x 10 cm^2, whereas the beam energy was 6 MV. The phantom's area was around 20 x 20 cm^2 enough to provide lateral electronic equilibrium. A value of 3.5 ms was selected for the integration time and 10000 for the number of frames at each measuring position. The former means that one complete pulse of radiation will be recorded per frame with the LINAC pulse repetition frequency being 300 Hz[♣] for a dose rate setting of 600 MU/min, as chosen for our measurements. Finally, the measurements were repeated with the use of an ionisation chamber as a benchmark and to highlight any deviations. The results of the PDD measurements are presented in Figure 32.

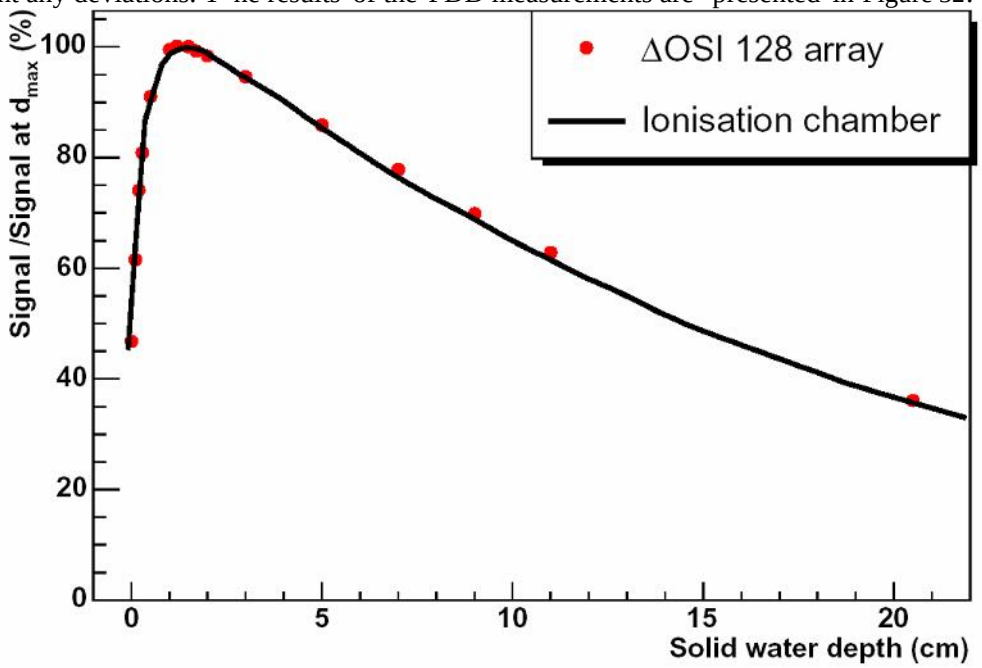

Figure 32 Percentage Dose Distribution for 6 MV X-rays, at 100 cm SSD, for 10x10 cm^2 field measured with the project's detector (?ODI 128) and one of Weston Park's standard ionisation chambers, see text for details.

A linear interpolation has been used to produce the continuous curve for the ionisation chamber data. Nonetheless, the agreement between the PDD data measured with this project's dosimeter and those taken with the ionisation chamber is evident. The largest difference between the two sets of data was less than 1%. More importantly the depth of the maximum dose was found at 1.5 cm in agreement with previous measurements at the hospital and what is expected by 6 MV X-rays, for example see reference [17]. Finally, for completeness the statistical errors from the

[♣] Taken from the LINAC's user manual and verified by a direct measurement with a scope on the "TRIG" output port at the control console.

frame averaging at each measuring point are less than 0.3%, i.e. to small to be visible in the figure.

4.2.2 Beam Profile

The same set-up as in the previous section was used for the measurement of the beam penumbra with the only difference that a film replaced the ionisation chamber used as a benchmark. Likewise, the photon energy, dose rate, SSD, field size as well as the integration time and number of frames per measurement were the same. The penumbra was measured at a water equivalent depth of 5 cm, i.e. deeper than the point of maximum dose (1.5 cm), to allow for charge particle equilibrium conditions. A typical plot with the characteristic shape for the beam penumbra is shown in Figure 33.

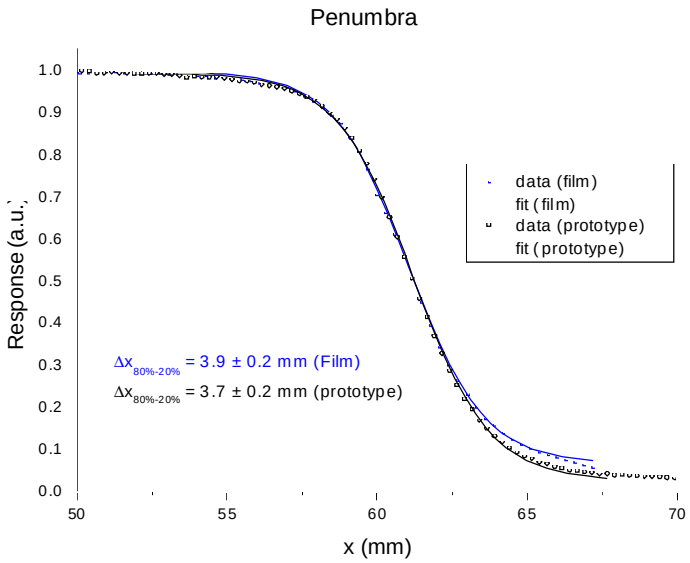

Figure 33 Beam penumbra for 6 MV X-rays, at 100 cm SSD, for 10x10 cm^2 field measured with the project's detector (DOSI 128) and Weston Park's standard (film).

For a direct comparison, the penumbrae measured with both systems (our prototype detector and the film) were normalised to the 50% point. The data were then fitted with a sigmoid function for the derivation of the 80%-20% dose points that we used to define the penumbra being the extent of the dose distribution between the 80% and 20% dose points. Note, that errors are included in the above figure but are too small to be visible (<0.2%). The calculated value for the "80-20" penumbra is in agreement with the one derived by the hospital standard dosimeter (film) within the errors of the measurement.

4.2.3 Dose Field Factors

The output factors were the final dosimetric quantity to be measured in this project. The set up was that of section 4.2.1 above (PDD measurements) with the main parameters those of 6 MV photons, 100 cm SSD, 600 MU/min, 3.5 ms integration time and 10 000 frames per measurement. The depth was again 5 cm for the reasons explained in the above. Finally, the field size varied in accordance with the definition of this quantity, given in previous chapter. Likewise, the reference field was chosen as 10x10 cm^2 in accordance with standard practice in the hospital. The following picture shows the results with our detector against those measured with an ionisation chamber.

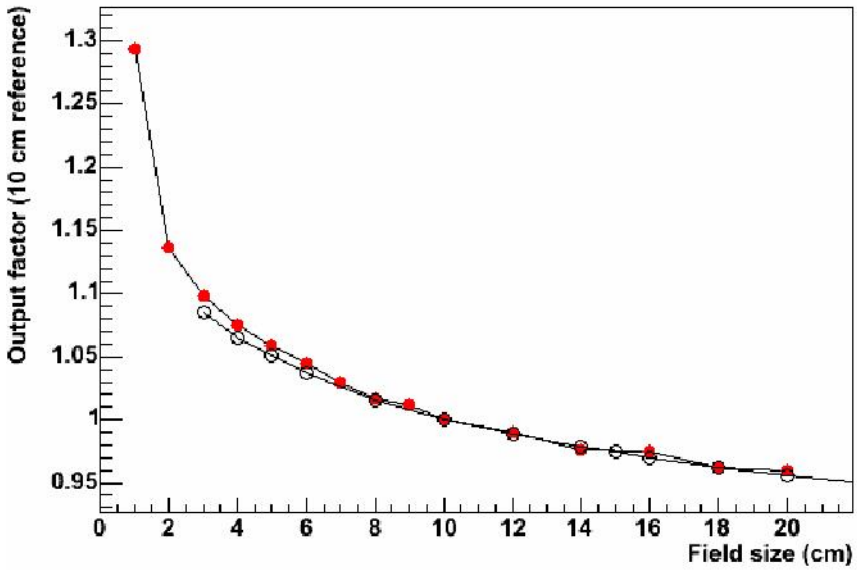

Figure 34 Output factors for various field sizes measured with our detector (red solid circles) and an ionisation chamber (black open circles)♦.

As shown in Figure 34, there is very good agreement between the two dosimeters, especially for larger fields, sizes greater than 8x8 cm^2. The agreement worsens progressively as the field size gets smaller, but it never exceeds 2%. However, the ionisation chamber is unable to provide reliable information for fields smaller than 3 cm, due to its size.

References

1. 487 picoammeter-voltage source user's manual, pub. Keithely instruments.
2. 4274A multi-frequency LCR user's manual, pub. Hewlett-Packard.
3. XDAS User manual, pub. Electron Tubes Ldt.
4. Rosenberg, Radiation physics with medical applications MSc lecture notes, UCL.

♦ Contrary to the definition given on the previous chapter, the values for output factors in the figure were calculated as the ratio of response for the reference field size over that for a particular size. Thus, they are the reciprocal of what is commonly encountered in the literature, as is the shape of the curve.

5 Conclusions

Radiation detectors play a crucial supporting role in all aspects of radiotherapy: a) in QA measurements to check the condition of equipment and b) to verify the delivery of the treatment plan. Modern radiotherapy modalities like IMRT utilise dynamic non uniform radiation fields to create complex 3D dose distributions that match closer to the treatment volume, thus keeping the dose to critical organs at a minimum [1]. This however imposes stringent demands on dosimetry with no single dosimeter commercially available at present that meets all requirements [2]. Similar requirements are encountered in small field dosimetry, as for example in stereotactic radiosurgery, with emphasis given in high spatial resolution and small detector size to account for dose distributions with steep gradients and lateral electronic disequilibrium. It should be noted that here (SRS) the demand for real time, dynamic measurements is not an available option at present. Nonetheless, such an option would have been a welcomed bonus, helping to alleviate the "time burden" and increase patient throughput for these highly sought modalities.

New detectors for radiotherapy dosimetry should measure all important quantities for QA measurements. Furthermore, for treatment planning verification they should be able for in-vivo measurements, for example by measuring the dose at the beam's exit from the patient (portal dose). It was hoped that the advent of electronic portal imaging devices (EPIDs) will finally make this possible [3]. However, although EPIDs are presently offered as standard equipment with any new Linac, they are not yet in common practice at NHS hospitals let alone have replaced the conventional detectors. This is because they have their own drawbacks, which include [4, 5]:

- Energy dependent response, because of the scintillator.
- Small signals, especially in camera based systems, mostly due to light losses by the optical components (mirror and lens).
- Spatial aberrations, mostly encountered in the camera systems due to the lens.
- Low spatial resolution due to light diffusion in the scintillator and the optical coupling, common to all indirect detection systems.
- "Salt and pepper" noise in the image as a result of radiation damage to the camera.
- Field size dependent response due to optical cross talk between multiple light reflections between mirror and lens (camera systems).
- Memory effects in TFT arrays ("on beam axis" systems), mostly those made by amorphous selenium technology.
- Slow read-out rates, especially in TFT arrays.

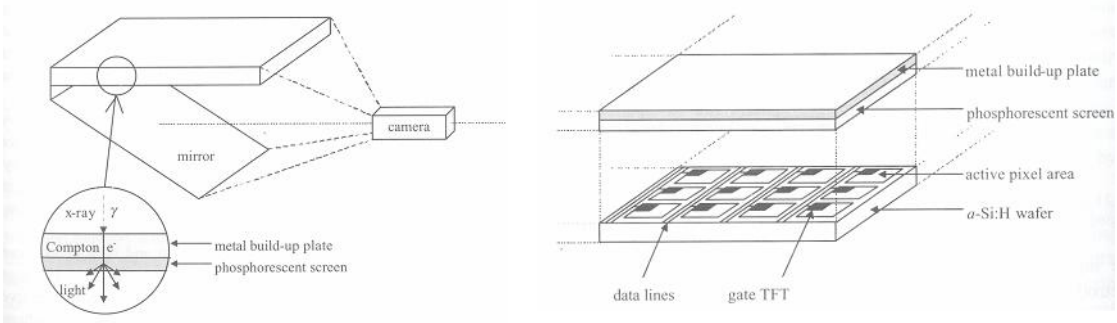

Figure 1 Electronic portal imaging devices: a) Camera based system (left) and b) right, a system using a flat panel TFT array [3].

The prototype detector evaluated in this project, looks very promising as dosimeter for radiotherapy applications. It was able to perform QA relevant tasks by measuring the quantities of interest. Specifically, during dosimetric measurements with 6 MV X-rays from a clinical Linac, it was shown that:

- The depth dose measurements, like PPDs, were as expected and in agreement with measurements made with an ionisation chamber.
- Off-axis measurements, like beam profiles, were as good as those with film in resolving the penumbra.
- Output factors, where measured for various field sizes in good agreement with an ionisation chamber. Moreover, it was possible to resolve fields smaller than 2 cm, i.e. much smaller than what is possible with an ionisation chamber.
- Finally, dynamic measurements were possible and in real time. Figure 2 below gives an example of a dose distribution (dynamic wedge) created by the appropriate motion of a MLC rather than a static wedge shaped collimator.

Based on these results, the work undertaken here should continue to further develop specialised dosimeters. Efforts should be taken to develop dedicated systems for QA or treatment planning verification. Linear arrays of larger size should be fabricated, able to measure all fields encountered in clinical cases, which could be up to 40 cm wide. With the processing of 12" (ca. 30 cm) silicon wafers being common practice for the microelectronics industry nowadays, this should be feasible. To maintain the same resolution even at the largest fields the number of pixels will increase with an accompanying burden in the read-out channels. Once more, the use of multichannel read-out electronic chips (ASICs) and powerful dedicated data acquisition systems should be utilised, as demonstrated in particle physics experiments, where one is able to cope with million of channels working at MHz rates.

The Technology Business Unit and CCLRC at a larger extent, is very well placed to undertake such a task due to its long experience in developing detector systems for particle physics experiments. Furthermore, TBU's detector division is already transferring knowledge created in PPD experiments. For example, the electronics used in this project are based on the XCHIP ASIC, originally developed for synchrotron radiation experiments [6], itself a "spin-off" of the highly successful MX family employed in PPD experiments for the last 20 years. Moreover, with the creation of the new council (STFUK) this is an ideal time for the exploitation of particle physics technology for the benefit of the general public.

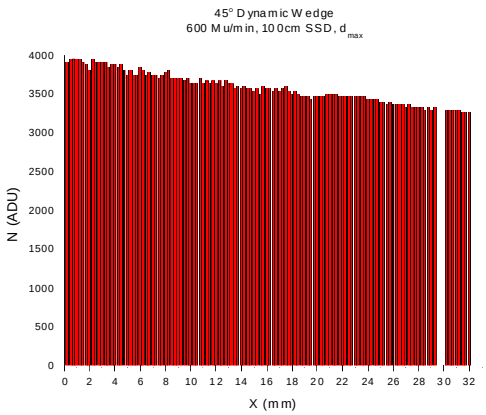

Figure 2 Dose distribution profile of a "Dynamic Wedge" created by moving MLC collimators ala dIMRT.

References

1. S. Webb, Intensity Modulated Radiotherapy, IOP Publishing (2001).
2. IMRT International Working Party, "IMRT: current status and issues of interest", Int. J. Rad. Onc. Biol. Phys., v51, No. 4 (2001) 880-914.
3. Ionising Radiation Detectors for Medical Imaging, A. Del Guerra, World Scientific, ISBN: 981-238-674-2.
4. S. Vieira et al., "Dosimetric verification of X-ray fields with steep dose gradients using EPIDs", Phys. Med. Biol. 48 (2003) 157-166.
5. P. Greer et al., "Dosimetric properties of an amorphous silicon EPID for verification of dynamic IMRT", Med. Phys. 30, 7 (2003) 1618-1627.
6. J. Headspith et al., "XSTRIP - a silicon microstrip based X-ray detector for ultra-fast X-ray spectroscopy studies", NIM A512 (2003) pp. 239-244.

Acknowledgements

The work in this paper was possible through funding by the Department of Health and the Particle Physics and Astronomy Research Council. The author would like to thank the members of the DOSI project for their support and close collaboration throughout and in particular: Dr. J. Conway of the Sheffield Teaching Hospitals NHS Trust for providing access to clinical Linacs, Dr. C. Buttar of the university of Glasgow for discussions and sharing of resources and Dr. S. Walsh (Micron Semiconductors Ltd.) and M. Homer (Electron Tubes Ltd.) for their in kind contribution to the project. Finally, special thanks go to Nathan Hill and Mark Littlewood of PPARC's KIT E Club for their help in securing funding in the first place...